

Nonlinear Material Design Using Principal Stretches

Hongyi Xu Univ. of Southern California Funshing Sin Univ. of Southern California
Blizzard Entertainment Yufeng Zhu Univ. of Southern California
Univ. of British Columbia Jernej Barbič Univ. of Southern California

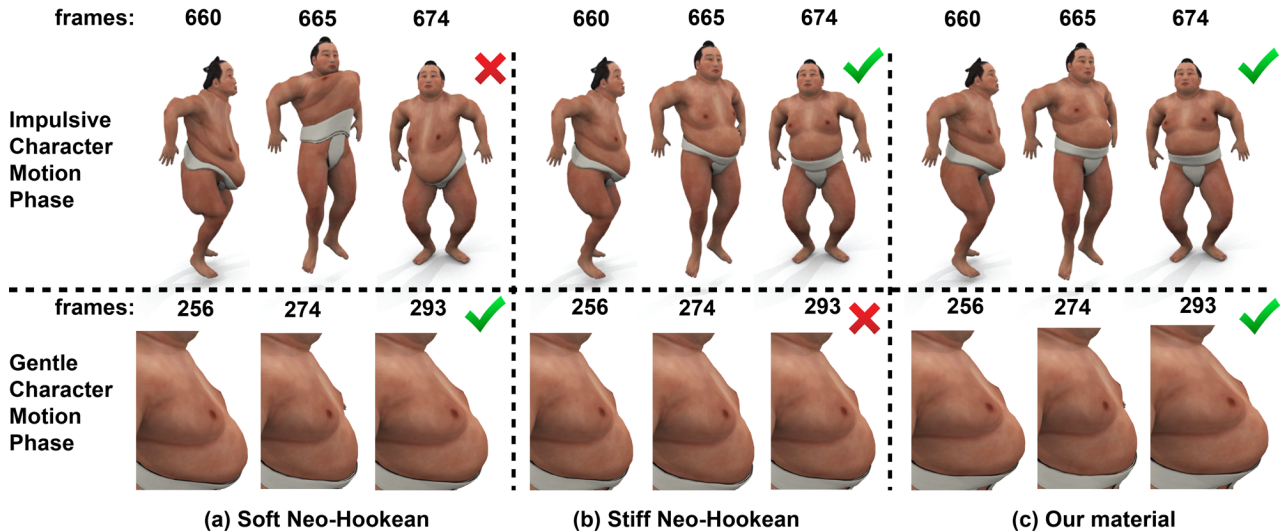


Figure 1: Design of isotropic nonlinear materials: The soft-body motion of the wrestler was computed using FEM, constrained to a motion capture skeletal dancing animation. Using our method, we designed a nonlinear isotropic material that performs well both during impulsive and gentle animation phases. Top row: the wrestler is performing high jumps. The soft Neo-Hookean material exhibits artifacts (belly, thighs) when the character moves abruptly. Our material and the stiff Neo-Hookean material produce good deformations. Bottom row: deformations during a gentle phase (walking while dancing) of the same motion sequence. The soft Neo-Hookean material and our method produce rich small-deformation dynamics, whereas the stiff Neo-Hookean material inhibits it. The Young’s modulus of material (a) was chosen to produce good dynamics during gentle motion. We then edited it to address impulsive motion, producing (c). The stiff material in (b) is the best matching material to (c) among Neo-Hookean materials, minimizing the L_2 material curve difference to (c).

Abstract

The Finite Element Method is widely used for solid deformable object simulation in film, computer games, virtual reality and medicine. Previous applications of nonlinear solid elasticity employed materials from a few standard families such as linear corotational, nonlinear St.Venant-Kirchhoff, Neo-Hookean, Ogden or Mooney-Rivlin materials. However, the spaces of all nonlinear isotropic and anisotropic materials are infinite-dimensional and much broader than these standard materials. In this paper, we demonstrate how to intuitively explore the space of isotropic and anisotropic nonlinear materials, for design of animations in computer graphics and related fields. In order to do so, we first formulate the internal elastic forces and tangent stiffness matrices in the space of the principal stretches of the material. We then demonstrate how to design new isotropic materials by editing a single stress-strain curve, using a spline interface. Similarly, anisotropic (orthotropic) materials can be designed by editing three curves, one for each material direction. We demonstrate that modifying these curves using our proposed interface has an intuitive, visual, effect on the simulation. Our materials accelerate simulation design and enable visual effects that are difficult or impossible to achieve with standard nonlinear materials.

CR Categories: I.3.5 [Computer Graphics]: Computational Geometry and Object Modeling—Physically based modeling, I.6.8 [Simulation and Modeling]: Types of Simulation—Animation

Links: [DL](#) [PDF](#) [WEB](#) [VIDEO](#)

Keywords: FEM, isotropic, anisotropic, material, design

1 Introduction

Three-dimensional solid Finite Element Method (FEM) simulations are widely used in computer graphics, animation and related fields. FEM simulations, however, are greatly influenced by the specific material relationship between the displacements (strains) and elastic forces (stresses). To date, applications in computer graphics use linear materials, or nonlinear materials where the strain-stress relationship is specified using a global equation, such as the linear corotational, St.Venant-Kirchhoff, Neo-Hookean, Ogden or Mooney-Rivlin materials [Bonet and Wood 1997; Bower 2011]. These materials, however, only scratch the surface of the space of all isotropic nonlinear elastic materials. The space of all anisotropic nonlinear materials is even broader. In order to more easily achieve complex visual effects, we approach the problem of how to model and de-

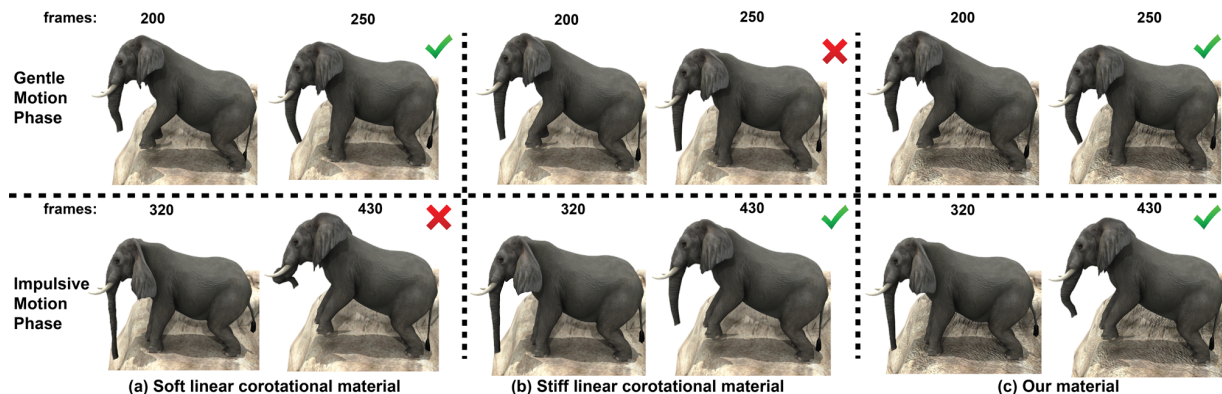


Figure 2: Jumping elephant. Two jump cycles are shown. (a) Soft corotational material can accommodate the flight phase well. During the hard ground impact, however, severe deformations occur in the trunk, ears and tail. (b) Stiff corotational material can handle hard ground impact, but produces almost no deformations during the rest of the motion. (c) Our material can accommodate all phases of the animation. The Young’s modulus of (a) was set so that the flight phase produces secondary motion comparable to (c). The Young’s modulus of (b) was set so that the maximum deformed trunk length is the same as in (c).

sign arbitrary nonlinear materials, for use in animations in computer graphics and related fields. We give a method to design isotropic and anisotropic (orthotropic) nonlinear solid elastic materials using a piecewise spline interface, and demonstrate its use on complex soft-body physically based simulations.

As a motivation, Hahn et al. [2013], which presented an efficient method for augmenting keyframed character motions with physically-simulated secondary motion, posed a challenge in their conclusion. “It can be cumbersome to find material parameters that yield soft behavior around the rest state but do not lead to excessive deformations for fast motion.” Our work addresses this challenge, by creating materials that are more versatile than standard global materials. Such materials can accommodate animations that contain both slow and gentle, and impulsive and energetic motions (Figures 1, 2). We note that the trivial solution of keyframing stiffness over time does not work (Figure 10) as the time-varying stiffness makes the system non-conservative and the material behaves like a muscle. Furthermore, some motions such as dancing in Figure 1 cannot be easily segmented for such keyframing.

Nonlinear isotropic materials correspond to symmetric elastic energy functions $\Psi(\lambda_1, \lambda_2, \lambda_3) : \mathbb{R}^3 \mapsto \mathbb{R}$, where λ_i are the singular values of the deformation gradient \mathbf{F} (the “principal stretches”). We note that energy functions can also be expressed in terms of the invariants of $\mathbf{C} = \mathbf{F}^T \mathbf{F}$, but stretch-based materials $\Psi(\lambda_1, \lambda_2, \lambda_3)$ are in practice more general because they can express all isotropic materials without any special numerical difficulty (Section 3). We therefore design our materials using stretch-based energies. The space of all symmetric functions $\Psi(\lambda_1, \lambda_2, \lambda_3)$ is vast and not easy to navigate. We simplify the space using the Valanis-Landel hypothesis [Valanis and Landel 1967], decoupling Ψ into three 1D scalar energy functions (Section 4.1). In most cases, we further simplify the energy, retaining a single 1D function. We model these 1D scalar functions using piecewise splines. Our splines give the 1D relationship between the uniaxial, biaxial or triaxial stretch and the resulting internal elastic force, providing local control over the stretch-force relationship. For example, the user can precisely adjust how rapidly the nonlinear material stiffens under tension, and how much it resists to various levels of compression. Our design generalizes to anisotropic (orthotropic) materials (Section 4.3). Although the goal of our system is to design virtual materials, our material model could also potentially be applied to parameter fitting applications.

We simulate our materials using the invertible nonlinear FEM [Irving et al. 2004], which decomposes the deformation gradient \mathbf{F} of each element using the singular value decomposition (SVD), and then computes the stress tensor using the singular values $\lambda_1, \lambda_2, \lambda_3$. Their scheme timesteps elastic forces explicitly; we demonstrate in Figure 4 (a) that implicit integration enables a $65\times$ larger stable timestep under equal simulation conditions. For energies defined using the invariants of \mathbf{C} , Teran et al. [Teran et al. 2005] developed a method to compute the stiffness matrix, enabling implicit integration. To accommodate the Valanis-Landel hypothesis, our simulator must work with stretch-based energies. Methods to compute the tangent stiffness matrix for such energies were previously proposed by [Gao et al. 2009] and [Stomakhin et al. 2012]. We present a method that stably simulates stretch-based materials using the gradient of SVD, introduced by Papadopoulos and Lourakis [2000] in another application domain. We demonstrate that our stretch-based simulator significantly outperforms [Gao et al. 2009] (Figure 4, (d)). It is also 33% faster than the method presented in [Stomakhin et al. 2012] (and $2.2\times$ for computing dP/dF). Our material design applies equally to all the three stretch-based simulation methods. Our contributions include:

- reduction of the space of all isotropic and orthotropic materials to a more manageable, but still expressible, subset suitable for user design,
- local stable design of materials using a spline-based editor,
- faster stable simulation of solid nonlinear materials expressed using principal stretches (Figure 3),
- a simulator and material design tool for nonlinear orthotropic solid materials.

2 Related Work

Deformable object simulation is a well-studied problem in computer graphics, and FEM is a commonly used method [Sifakis and Barbic 2012]. Linear models are the simplest FEM models, typically suitable for small deformations. Linear corotational FEM [Müller and Gross 2004] alleviates the problem of large deformations by extracting local material rotations using polar decomposition [Parker and O’Brien 2009; Chao et al. 2010; McAdams et al. 2011; Civit-Flores and Susin 2014]. However, under large compressions and tensions, this method still suffers from its linear material properties. Another common approach to model large defor-

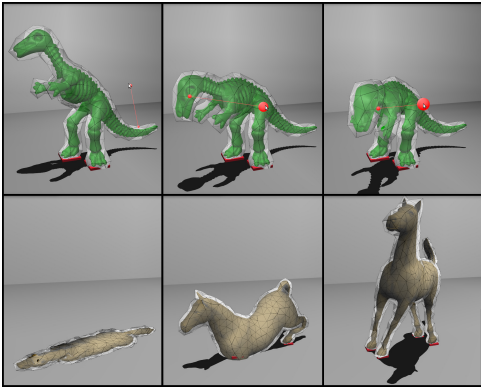


Figure 3: Stable principal stretch simulations using SVD gradients: Interactive dinosaur (1,031 tets, 344 vertices, 80 fps, Ogden). A horse collapses into a plane and recovers (1,963 tets, 758 vertices, 40 fps, linear corotational material).

mations is to use geometrically nonlinear models, for example, the isotropic St.Venant-Kirchhoff (StVK) material model [O’Brien and Hodgins 1999; Capell et al. 2002]. Our simulator accommodates arbitrary hyperelastic isotropic materials. Large deformations can be avoided with strain limiting constraints, which lock the strains to a given range [Perez et al. 2013; Hernandez et al. 2013]. Our method makes it possible to penalize large strains with arbitrary, user-designed forces that are integrable and require no modifications to the integration scheme.

Material design and optimization: Standard isotropic materials in computer graphics all involve some material constants to be determined, with global effect on the strain-stress relationship. We model the material using a piecewise spline representation. A similar approach has been proposed in the engineering community for incompressible materials and fitting materials to experimental data [Sussman and Bathe 2009], whereas we pursue compressible materials and animator material design. Compressible materials are commonly used with standard implicit integrators in computer graphics, and we can still enforce quasi-incompressibility using volume preservation energy terms. In comparison to standard global materials, the spline material representation allows us to edit the material locally, which permits greater design freedom and improves stability. Several authors obtain material parameters by measuring real objects, such as Young’s modulus and/or Poisson’s ratio [Becker and Teschner 2007; Bickel et al. 2009; Lee and Lin 2012], cloth parameters [Wang et al. 2011] and facial muscle activations [Sifakis et al. 2005]. Our spline nonlinear model could also be used to fit a material based on captured data, similar, e.g., to [Sussman and Bathe 2009]. Material optimization for space-time motion editing has been recently explored by [Li et al. 2014]. However, their method does not output world-space materials, but gives the output materials implicitly, by changing global linear modes and frequencies. Our method provides an explicit nonlinear material model, making it possible to apply our materials to arbitrary meshes and motions.

Anisotropic materials are discussed in many references [Bonet and Burton 1998; Bower 2011]. Linear and nonlinear FEM models have been explored to simulate transversely isotropic materials [Picinbono et al. 2001; Ten Thije et al. 2007] and have been widely used in medical simulation of soft tissues [Allard et al. 2009], electro-mechanical heart [Talbot et al. 2013] and human muscles [Teran et al. 2005; Sifakis et al. 2005]. However, all of these previous solid anisotropic applications in computer graphics focused on transversely isotropic materials where two directions have equal stiffness. Orthotropic materials generalize transversely

isotropic materials, by exhibiting different stiffnesses in three orthogonal directions. Linear corotational orthotropic material modeling has been presented in [Li and Barbič 2014] by directly setting the parameters of the elasticity tensor. Different from them, we give a method for nonlinear orthotropic material modeling and design.

3 Invertible Principal-Stretch Materials

In this section, we describe our principal stretch-based FEM method to compute the elastic forces and tangent stiffness matrices of stretch-based materials $\Psi(\lambda_1, \lambda_2, \lambda_3)$. We note that alternatively, the strain energy may be expressed in terms of the invariants

$$I_C = \text{trace}(\mathbf{C}) = \lambda_1^2 + \lambda_2^2 + \lambda_3^2, \quad III_C = \det(\mathbf{C}) = \lambda_1^2 \lambda_2^2 \lambda_3^2, \quad (1)$$

$$II_C = \mathbf{C} : \mathbf{C} = \lambda_1^4 + \lambda_2^4 + \lambda_3^4. \quad (2)$$

We initially considered modeling materials as $\Psi(I_C, II_C, III_C)$, as both approaches are theoretically equivalent. However, some materials, in particular those that involve odd powers of λ_i , are difficult to model as $\Psi(I_C, II_C, III_C)$. For example, the linear corotational model is given as $\Psi = \frac{1}{2} \lambda_{\text{Lamé}} (i_C - 3)^2 + \mu_{\text{Lamé}} (ii_C - 2i_C + 3)$, where $i_C = \lambda_1 + \lambda_2 + \lambda_3$, $ii_C = \lambda_1^2 + \lambda_2^2 + \lambda_3^2$, $iii_C = \lambda_1 \lambda_2 \lambda_3$. At first, it seems that one could express λ_i or i_C, ii_C, iii_C in terms of I_C, II_C, III_C and thus still support arbitrary energies using the invariant simulator [Teran et al. 2005]. However, this requires solving for the roots of a cubic polynomial and differentiating them with respect to the deformation gradient, which introduces stability problems; we demonstrate this in Figure 4 (c). Furthermore, the Valanis-Landel hypothesis (Section 4.1) is applicable to stretch-based materials, and extends easily to orthotropic materials. For these reasons, we model our materials in the stretch-space $\Psi(\lambda_1, \lambda_2, \lambda_3)$.

3.1 Force Computation

Following Irving’s work [Irving et al. 2004], we compute the tetrahedron force on a vertex i as $\mathbf{g}_i = -\mathbf{P}\mathbf{b}_i$, where $\mathbf{P} \in \mathbb{R}^{3 \times 3}$ is the first Piola-Kirchhoff stress, $\mathbf{b}_i = (A_1 \mathbf{N}_1 + A_2 \mathbf{N}_2 + A_3 \mathbf{N}_3)/3$, and $A_j \mathbf{N}_j$ are the area-weighted material normals. The vertex forces in a single tetrahedron are $\mathbf{G} = \mathbf{P}\mathbf{B}_m$, where $\mathbf{G} = (\mathbf{g}_1, \mathbf{g}_2, \mathbf{g}_3)$, and $\mathbf{B}_m = (\mathbf{b}_1, \mathbf{b}_2, \mathbf{b}_3)$. The stress tensor \mathbf{P} can be computed as

$$\mathbf{P} = \mathbf{P}(\mathbf{F}) = \mathbf{U}\mathbf{P}(\hat{\mathbf{F}})\mathbf{V}^T, \quad (3)$$

where $\mathbf{F} = \mathbf{U}\hat{\mathbf{F}}\mathbf{V}^T$ is the SVD of \mathbf{F} , and $\text{diag}(\hat{\mathbf{F}}) = (\lambda_1, \lambda_2, \lambda_3)$.

3.2 Tangent Stiffness Matrix Computation

The gradient of the elastic force of a tetrahedron is:

$$\frac{\partial \mathbf{G}}{\partial \mathbf{u}} = \frac{\partial \mathbf{G}}{\partial \mathbf{F}} \frac{\partial \mathbf{F}}{\partial \mathbf{u}} = \left(\frac{\partial \mathbf{P}}{\partial \mathbf{F}} \mathbf{B}_m \right) \frac{\partial \mathbf{F}}{\partial \mathbf{u}} \in \mathbb{R}^{9 \times 12}, \quad (4)$$

where $\mathbf{u} \in \mathbb{R}^{12}$ is the displacement of the vertices, and $\partial \mathbf{F}/\partial \mathbf{u}$ and \mathbf{B}_m are constant matrices during the simulation. The force gradient of the remaining vertex is $\partial \mathbf{g}_0/\partial \mathbf{u} = -(\partial \mathbf{g}_1/\partial \mathbf{u} + \partial \mathbf{g}_2/\partial \mathbf{u} + \partial \mathbf{g}_3/\partial \mathbf{u})$. We need to compute $\partial \mathbf{P}/\partial \mathbf{F}$. Because \mathbf{P} is defined using SVD, we differentiate SVD using the product rule,

$$\frac{\partial \mathbf{P}}{\partial \mathbf{F}_{ij}} = \frac{\partial \mathbf{U}}{\partial \mathbf{F}_{ij}} \mathbf{P}(\hat{\mathbf{F}}) \mathbf{V}^T + \mathbf{U} \frac{\partial \mathbf{P}(\hat{\mathbf{F}})}{\partial \mathbf{F}_{ij}} \mathbf{V}^T + \mathbf{U} \mathbf{P}(\hat{\mathbf{F}}) \frac{\partial \mathbf{V}^T}{\partial \mathbf{F}_{ij}}. \quad (5)$$

We note that such SVD gradient was previously explored for applications in computer vision [Papadopoulos and Lourakis 2000]. In computer graphics, Twigg and Kačič-Alesić [2010] explored similar gradients for constraint simulation, but ultimately only needed

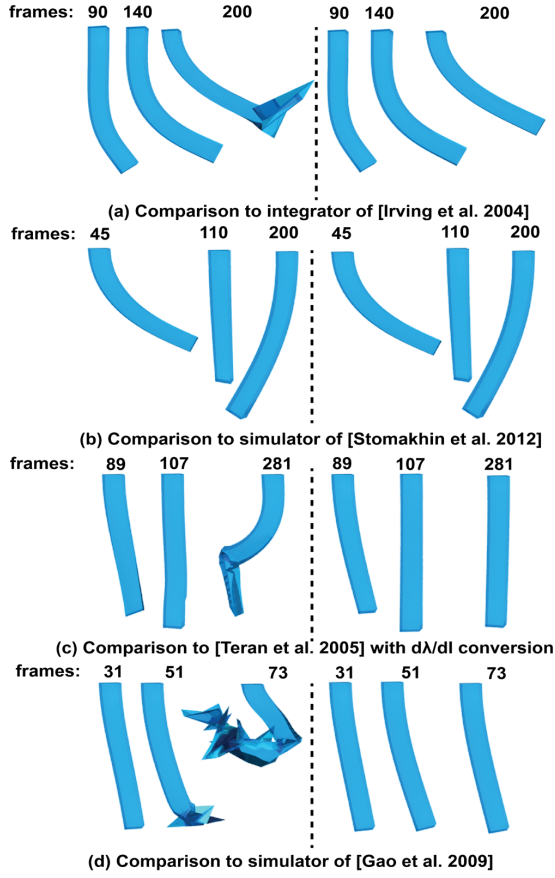


Figure 4: Comparison to alternative FEM simulators: (a) Left: integration scheme of [Irving et al. 2004], right: implicit backward Euler integrator. Neo-Hookean material. The implicit integration is $65\times$ more stable. (b) Left: stretch-based simulator of [Stomakhin et al. 2012], right: our SVD gradient stretch-based method (33% faster with the same stability). Linear corotational material. No visual difference is observed. (c) Left: invariant-based method [Teran et al. 2005], right: our principal-stretch-based method ($1000\times$ more stable and $3.6\times$ faster). Linear corotational material. (d) Left: method of [Gao et al. 2009], right: our method using SVD gradient ($5\times$ more stable and $35\times$ faster). Ogden material.

and computed gradients of $\mathbf{R} = \mathbf{U}\mathbf{V}^T$, not individual gradients of \mathbf{U} and \mathbf{V} . SVD gradients were previously also employed for strain-limiting simulations [Hernandez et al. 2013]. We need to compute $\partial\mathbf{U}/\partial\mathbf{F}_{ij}$, $\partial\mathbf{P}(\hat{\mathbf{F}})/\partial\mathbf{F}_{ij}$, and $\partial\mathbf{V}^T/\partial\mathbf{F}_{ij}$. In order to do so, we differentiate SVD with respect to \mathbf{F}_{ij} and then multiply \mathbf{U}^T and \mathbf{V} on the left and right, respectively. This yields

$$\begin{aligned} \mathbf{U}^T \left(\frac{\partial\mathbf{F}}{\partial\mathbf{F}_{ij}} \right) \mathbf{V} &= \mathbf{U}^T \left(\frac{\partial\mathbf{U}}{\partial\mathbf{F}_{ij}} \hat{\mathbf{F}} \mathbf{V}^T + \mathbf{U} \frac{\partial\hat{\mathbf{F}}}{\partial\mathbf{F}_{ij}} \mathbf{V}^T + \mathbf{U} \hat{\mathbf{F}} \frac{\partial\mathbf{V}^T}{\partial\mathbf{F}_{ij}} \right) \mathbf{V} = \\ &= \left(\underbrace{\mathbf{U}^T \frac{\partial\mathbf{U}}{\partial\mathbf{F}_{ij}}}_{\tilde{\omega}_U^{ij}} \right) \hat{\mathbf{F}} + \frac{\partial\hat{\mathbf{F}}}{\partial\mathbf{F}_{ij}} + \hat{\mathbf{F}} \left(\underbrace{\frac{\partial\mathbf{V}^T}{\partial\mathbf{F}_{ij}} \mathbf{V}}_{\tilde{\omega}_{V^T}^{ij}} \right). \end{aligned} \quad (6)$$

Note that $\partial\mathbf{F}_{mn}/\partial\mathbf{F}_{ij} = 0$ when $(m,n) \neq (i,j)$, and 1 otherwise. Matrices $\tilde{\omega}_U^{ij}$ and $\tilde{\omega}_{V^T}^{ij}$ are antisymmetric. Since $\hat{\mathbf{F}} \in \mathbb{R}^{3 \times 3}$ is a diagonal matrix and the diagonal elements of $\tilde{\omega}_U^{ij} \hat{\mathbf{F}}$ and $\hat{\mathbf{F}} \tilde{\omega}_{V^T}^{ij}$ are zero,

the three unknown entries of the diagonal matrix $\partial\hat{\mathbf{F}}/\partial\mathbf{F}_{ij}$ can be set to the diagonal of the resulting matrix on the left hand side,

$$\text{diag}(\partial\hat{\mathbf{F}}/\partial\mathbf{F}_{ij}) = \text{diag}(\mathbf{U}^T (\partial\mathbf{F}/\partial\mathbf{F}_{ij}) \mathbf{V}). \quad (7)$$

The elements of $\tilde{\omega}_U^{ij}$ and $\tilde{\omega}_{V^T}^{ij}$ can be computed by solving three 2×2 symmetric systems:

$$\begin{bmatrix} \lambda_l & \lambda_k \\ \lambda_k & \lambda_l \end{bmatrix} \begin{bmatrix} (\tilde{\omega}_U^{ij})_{kl} \\ (\tilde{\omega}_{V^T}^{ij})_{kl} \end{bmatrix} = \begin{bmatrix} u_{ik} v_{jl} \\ -u_{il} v_{jk} \end{bmatrix}, \quad (8)$$

where $k, l = 1, 2, 3$, $(\cdot)_{kl}$ is the matrix element (k, l) , $u_{ik} = (\mathbf{U})_{ik}$, and $v_{jk} = (\mathbf{V})_{jk}$. Finally, we compute $\partial\mathbf{U}/\partial\mathbf{F}_{ij}$ and $\partial\mathbf{V}^T/\partial\mathbf{F}_{ij}$ as:

$$\frac{\partial\mathbf{U}}{\partial\mathbf{F}_{ij}} = \mathbf{U} \tilde{\omega}_U^{ij}, \quad \frac{\partial\mathbf{V}^T}{\partial\mathbf{F}_{ij}} = \tilde{\omega}_{V^T}^{ij} \mathbf{V}^T. \quad (9)$$

The system in (8) becomes ill-conditioned if $\lambda_k \approx \lambda_l$. Moreover, SVD is not even unique in such degenerate cases, and randomly returns \mathbf{U} and \mathbf{V} within the space of multiple singular vectors, which can introduce noticeable error in the stiffness matrix computation. To resolve this problem, we perturb the λ_k, λ_l with $\varepsilon/2$ (we use $\varepsilon = 10^{-6}$) when $\|\lambda_k - \lambda_l\| < \varepsilon$. Then we perform SVD again on the perturbed deformation gradient $\tilde{\mathbf{F}} = \mathbf{U} \tilde{\Sigma} \mathbf{V}^T$. This yields new matrices $\tilde{\mathbf{U}}$ and $\tilde{\mathbf{V}}$ and use them in the SVD gradient computation afterwards; note that the elastic force computation uses the original λ_i . Matrices $\tilde{\mathbf{U}}$ and $\tilde{\mathbf{V}}$ can be considered as the limit singular vector matrices as SVD approaches the degenerate case. Furthermore, (8) is always well-conditioned due to the perturbation and therefore no special handling is needed to solve it. Although recomputation of SVD is required at degenerated configurations, this only imposes a small computational overhead. Because degeneracy typically occurs only at sparse frames and elements, the SVD recomputation introduced only 1.3% computational overhead on average. To reduce the computation time, one could even cache the stiffness matrix at the rest configuration, which is by far the most common degenerate case. Since the energy density function Ψ is continuous, perturbation of $\hat{\mathbf{F}}$ does not introduce a significant error and visually did not make any difference in the simulation (Figure 4 (b)). We measured the relative error of our St.Venant-Kirchhoff stiffness matrix at the origin to be under machine precision when compared to the ground truth of a linear FEM material.

With $\partial\hat{\mathbf{F}}/\partial\mathbf{F}_{ij}$, $\partial\mathbf{U}/\partial\mathbf{F}_{ij}$ and $\partial\mathbf{V}^T/\partial\mathbf{F}_{ij}$ known, we can now evaluate Equation 5. The only remaining term is

$$\frac{\partial\mathbf{P}(\hat{\mathbf{F}})}{\partial\mathbf{F}_{ij}} = \frac{\partial\mathbf{P}(\hat{\mathbf{F}})}{\partial\hat{\mathbf{F}}} \frac{\partial\hat{\mathbf{F}}}{\partial\mathbf{F}_{ij}} = \sum_{d=1}^3 \frac{\partial\mathbf{P}(\hat{\mathbf{F}})}{\partial\lambda_d} \frac{\partial\lambda_d}{\partial\mathbf{F}_{ij}}, \quad (10)$$

where $\partial\lambda_d/\partial\mathbf{F}_{ij}$ are the diagonal entries of $\partial\hat{\mathbf{F}}/\partial\mathbf{F}_{ij}$. Derivative $\partial\mathbf{P}(\hat{\mathbf{F}})/\partial\lambda_d = \partial^2\Psi/\partial\lambda_d^2$ is the Hessian of the elastic energy. We will compute it analytically for our separable material models in Section 4.1.

4 Nonlinear Material Design

The isotropic hyperelastic materials in finite element analysis are usually given in terms of one of the standard analytical models such as the St.Venant-Kirchhoff, Neo-Hookean, Ogden and Mooney-Rivlin models [Bonet and Wood 1997; Bower 2011]. The common characteristic of these material models is that they are global functions of I_C, II_C, III_C or $\lambda_1, \lambda_2, \lambda_3$, parameterized by some material constants. These material constants constitute the degrees of freedom of the corresponding material space. Given the desired

stress-strain curves which determine the material behavior, the constants can be fitted to best represent the material behavior over the global strain range. In our work, we give animators greater local control by defining and simulating *local materials*. Our materials are defined as piecewise splines in the space of the stretches λ_i . Much like splines make it easier to design 3D curves, our material splines simplify the design of materials. They make it possible to create materials whose resistance to stretching grows arbitrarily. It is possible to create materials that behave linearly under small deformations, but stiffen in a controllable way under further stretching. Unlike with standard global models, our compression behavior is decoupled from tension and can be tuned separately.

4.1 Separable Elastic Strain Energy

In an isotropic material, the material properties are not dependent on the direction and therefore the strain energy density function $\Psi(\lambda_1, \lambda_2, \lambda_3)$ is symmetric with respect to the principal stretches $\lambda_1, \lambda_2, \lambda_3$, i.e., $\Psi(\lambda_{i_1}, \lambda_{i_2}, \lambda_{i_3}) = \Psi(\lambda_1, \lambda_2, \lambda_3)$ for any permutation (i_1, i_2, i_3) of $(1, 2, 3)$. It is, however, tedious to design and edit such symmetric three-dimensional scalar functions Ψ directly. Instead, we simplify the design by assuming that Ψ takes the form

$$\Psi(\lambda_1, \lambda_2, \lambda_3) = f(\lambda_1) + f(\lambda_2) + f(\lambda_3) + g(\lambda_1 \lambda_2) + g(\lambda_2 \lambda_3) + g(\lambda_3 \lambda_1) + h(\lambda_1 \lambda_2 \lambda_3), \quad (11)$$

where f, g, h are one-dimensional (nonlinear) scalar elastic strain energy density functions for uniaxial (length), biaxial (area), and triaxial strain (volume), respectively. Assumption 11 is known as Valanis-Landel hypothesis and was proposed and studied in engineering [Mooney 1940; Carmichael and Holdaway 1961; Valanis and Landel 1967], typically for rubber-like incompressible materials, where g and h are discarded. It can cover a very board range of isotropic materials and can express many standard global material models, such as the St.Venant-Kirchhoff, Neo-Hookean and linear corotational materials (Appendix A).

When an energy density function contains terms that couple two or more of f, g, h , such as $\lambda_1 \lambda_2^2 + \lambda_1 \lambda_3^2 + \lambda_2 \lambda_1^2 + \lambda_2 \lambda_3^2 + \lambda_3 \lambda_1^2 + \lambda_3 \lambda_2^2$, Assumption 11 will not hold. Such materials, however, are not so commonly useful in practice. Although Assumption 11 reduces the expressible isotropic material space, the gain is significant: we reduce the space of all symmetric three-dimensional scalar functions into the space of triples of one-dimensional functions, which makes the material design much easier and more intuitive. Furthermore, we often need to model only one of these three functions.

We now evaluate $\mathbf{P}(\hat{\mathbf{F}})$ and $\partial \mathbf{P}(\hat{\mathbf{F}}) / \partial \lambda_d$, for use in Equation 10. As argued by [Irving et al. 2004], diagonal $\hat{\mathbf{F}}$ yields diagonal stress

$$\mathbf{P}(\hat{\mathbf{F}}) = \text{diag} \left(\frac{\partial \Psi}{\partial \lambda_1}, \frac{\partial \Psi}{\partial \lambda_2}, \frac{\partial \Psi}{\partial \lambda_3} \right). \quad (12)$$

Using Equation 11, we obtain

$$\frac{\partial \Psi}{\partial \lambda_1} = f'(\lambda_1) + g'(\lambda_1 \lambda_2) \lambda_2 + g'(\lambda_3 \lambda_1) \lambda_3 + h'(\lambda_1 \lambda_2 \lambda_3) \lambda_2 \lambda_3. \quad (13)$$

This formula is symmetric with respect to λ_2 and λ_3 . Expressions for $\partial \Psi / \partial \lambda_2$ and $\partial \Psi / \partial \lambda_3$ can be obtained by relabeling $(1, 2, 3)$ to $(2, 3, 1)$ and $(3, 1, 2)$, respectively. Thus, given the derivative functions f', g', h' , the strain energy density gradients $\partial \Psi / \partial \lambda_i$ are uniquely determined. Because we must have $\Psi = 0$ at the rest configuration ($\lambda_1 = \lambda_2 = \lambda_3 = 1$), selecting specific functions f', g', h' also uniquely determines Ψ and therefore the material properties.

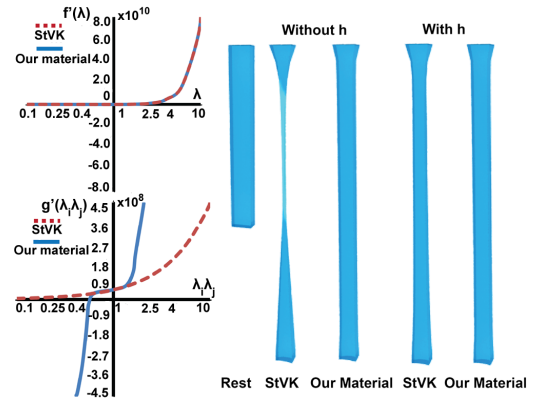


Figure 5: Editing g' : We edited the StVK material to increase the slope of the g' curve under large tension. Both materials have the same f' and h' curves. The x-axes give the principal stretch (top) and stretch products (bottom); note that the principal stretch axes are shown in the log-space in this paper, but the displayed ticks give the absolute value of λ . The beam deforms under gravity. Our material preserves the surface area better than StVK while keeping the stretched length approximately equal, which is not achievable by only tuning the f' curve. When volume preservation h is enabled (Equation 16), the effect of tuning the g' curve is less noticeable.

The second derivatives, needed for the stiffness matrix, are

$$\frac{\partial^2 \Psi}{\partial \lambda_1^2} = f''(\lambda_1) + g''(\lambda_1 \lambda_2) \lambda_2^2 + g''(\lambda_3 \lambda_1) \lambda_3^2 + h''(\lambda_1 \lambda_2 \lambda_3) \lambda_2^2 \lambda_3^2 \quad (14)$$

$$\frac{\partial^2 \Psi}{\partial \lambda_1 \lambda_2} = g''(\lambda_1 \lambda_2) \lambda_1 \lambda_2 + g'(\lambda_1 \lambda_2) + h''(\lambda_1 \lambda_2 \lambda_3) \lambda_1 \lambda_2 \lambda_3^2 + h'(\lambda_1 \lambda_2 \lambda_3) \lambda_3. \quad (15)$$

Expressions for the other second derivatives can be obtained by re-labeling indices, in the same way as in Equation 13.

Stability: Generally, a hyperelastic material model should satisfy the Hill's stability criterion (also called Drucker's condition), which requires a monotonic increase of strain energy density with increase in strain [Drucker 1957], $d\sigma : d\epsilon \geq 0$, where σ is stress and ϵ is strain. Violation of this condition usually leads to numerical failure. Similarly to [Sussman and Bathe 2009] who worked with incompressible materials, we adopt a related condition expressed in the space of principal stretches, but for compressible materials. The condition requires that the 3×3 matrix $\partial^2 \Psi / \partial \lambda^2$ must be positive-definite for the entire range of λ . The condition is difficult to enforce for general functions f, g, h . Instead, we consider the special case where $g = h = 0$. The condition then simplifies to $f''(x) > 0$, i.e., f' is a strictly increasing function. In practice, when adding g and h , we similarly require $g''(x) > 0$, $h''(x) > 0$, which gives increasing forces under increasing strain. We note that an alternative stability condition in literature uses polyconvexity of the energy function [Ball 1976]. Polyconvexity can guarantee the existence of elastic potential minima. Such conditions are, however, mathematically very complex. Our conditions are simple, easy to enforce, and have proven to work well in practice.

4.2 Spline Isotropic Materials

Assumption 11 decouples the strain energy density function into three 1D energy functions where all the variables have intuitive physical meanings. We design our materials by modeling the one-

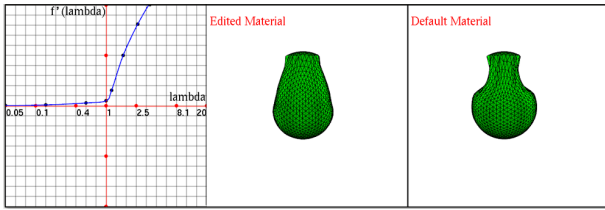


Figure 6: User interface for material design and simulation: *Left: spline material curve (f') design. User can drag/add/delete the control points (samples of f'). Middle: simulation using the current material. Right: simulation using the default (input) material (in this case Neo-Hookean). In the supplementary material video, we demonstrate that our spline editing works well even with a very small number of spline segments.*

dimensional scalar functions $f'(x), g'(x), h'(x)$, using splines. We choose to model the derivatives f', g', h' (the “force”) as opposed to directly the f, g, h (the “energy”). Compared to the strain energy density which is an abstract concept, stress (or the force) is more intuitive to understand and the derivative curves f', g', h' are directly related to stress via Equation 13. Also, in order to satisfy our stability criterium (previous paragraph), the user only has to ensure that the curves f', g', h' are increasing, a condition that is easier for the user to achieve than directly controlling a second derivative of f, g, h . When the condition is violated, we warn the user via a screen message. Derivative f' describes the stress due to the uniaxial tension and compression of the material. Quantity $g'\lambda_j$ gives the stress along axis i , originating due to the area change in plane ij , when the material deforms along axis i , but not along axis j . With λ_j fixed, the stress is linear in g' and we therefore only need to adjust g' . Similarly, $h'\lambda_j\lambda_k$ is stress on axis i originating due to the volume change when the material deforms along axis i , but not along axes j or k . Based on the same principle, we only need to adjust the curve h' . The derivatives of f', g', h' describe how fast the material stiffens as it stretches and compresses. This makes it possible to precisely control how rapidly (or slowly) the material stiffens (or weakens) under tension or compression, a capability that cannot be achieved with standard global material models.

In practice, we found that the f' curve is the most useful, as it is capable to tune most of the dynamic effects. Although curves g' and h' are also useful (see Figure 5), most effects of tuning curves g', h' can be achieved by editing f' . We note that we always add a compression resistance term [Kikuuwe et al. 2009] to h ,

$$h += \frac{\kappa}{12} \left(\frac{1-J}{6} \right)^3 \quad \text{if } J < 1, \text{ and } 0 \text{ otherwise,} \quad (16)$$

where κ is the compression resistance coefficient and $J = \lambda_1\lambda_2\lambda_3$. The compression resistance term helps preserve volume and increases simulation robustness. In the following, we only describe the editing of f' , whereas we typically leave g' and h' at their default material expressions. For example, when we start the design with the Neo-Hookean material, we use $g'(x) = 0$, and $h'(x) = (-\mu_{\text{Lamé}} + \lambda_{\text{Lamé}} \log x)/x$, where $\lambda_{\text{Lamé}}$ and $\mu_{\text{Lamé}}$ are the Lamé coefficients. If needed, g' and h' can be edited using the same procedure as f' .

In an interactive process, the user provides samples $(x_k, f'(x_k))$ for $1 \leq k \leq m$, over a chosen range $[\lambda_{\min}, \lambda_{\max}]$, for some user-chosen abscissas $x_k \in \mathbb{R}$. We then obtain a global function f' using piecewise Bézier spline interpolation and extrapolation. Details are provided in Appendix B. Our piecewise splines pass through all the samples, unlike standard global models that may incur a fitting error. In order to decrease the fitting error, one could employ a global material with a larger number of DOFs, such as the Ogden mate-

rial [Ogden 1997]

$$\Psi = \sum_{p=1}^N \frac{\mu_p}{\alpha_p} (\lambda_1^{\alpha_p} + \lambda_2^{\alpha_p} + \lambda_3^{\alpha_p}), \quad f(x) = \sum_{p=1}^N \frac{\mu_p}{\alpha_p} x^{\alpha_p}. \quad (17)$$

In Figure 7, we compare our splines to the Ogden material. It can be seen that the Ogden material produces curves with negative slopes, resulting in simulation instabilities. This is especially problematic in our design application where the users may place the samples $(x_k, f'(x_k))$ arbitrarily. Because the entire fitted Ogden material curve changes when one adjusts a sample, our spline interface offers a more direct and easier control over stability.

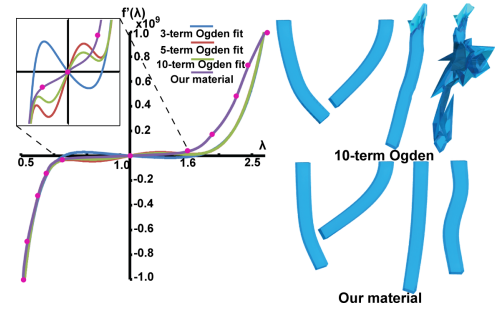


Figure 7: Comparison to fitting a global material model: *We fitted 3-, 5- and 10-term Ogden materials to representative (stretch, force) user input samples. Even with 20 material constants for the 10-term Ogden, the Ogden curve does not fit the data well in the tension region. The Ogden curves all produce undesirable oscillations in the small-strain region, resulting in unstable simulations. Our spline method does not have any fitting error and provides an increasing curve, resulting in stable simulations.*

In our system, the user directly edits the curve by moving the sample points in both x and y , and there is no need to provide the tangents since a_k, b_k are automatically constructed. Note that our spline editing system is not limited to Bézier splines and could employ other forms of splines. The samples can be moved freely, but all the samples must be increasing in both x and y directions; if they are not, we visually warn the user or prevent the sample adjustment. We initially tried fixed, non-editable abscissas x_k , but found them inconvenient as one frequently wants to make the material more (or less) stiff, which requires moving the abscissas x_k to cover a different range of λ . With Bézier interpolation of f' , the gradient of Ψ is C_1 -continuous, whereas the Hessian is C_0 -continuous (Appendix B). Although the energy $\Psi(\lambda)$ itself is not required for our simulation, we can always obtain it using numerical integration; it is C_2 -continuous.

4.3 Orthotropic Nonlinear Material Design

In contrast to isotropic materials, anisotropic materials exhibit different mechanical properties in different directions. For anisotropic materials, Assumption 11 does not hold as f, g, h need to incorporate the material directions, not just the value of λ itself. However, we can easily extend our framework to orthotropic materials. Orthotropic materials are a common class of anisotropic materials frequently employed in engineering. They exhibit three different material behaviors along three orthogonal axes [Li and Barbič 2014], and generalize isotropic and transversely isotropic materials. Excluded in the orthotropic family are anisotropic effects such as a normal force in a material direction causing a sideways shear, but these effects are not commonly needed in practice. Prior work investigated linear orthotropic materials [Li and Barbič 2014], whereas we design *nonlinear* orthotropic materials. We denote the three material axes along which the different material properties

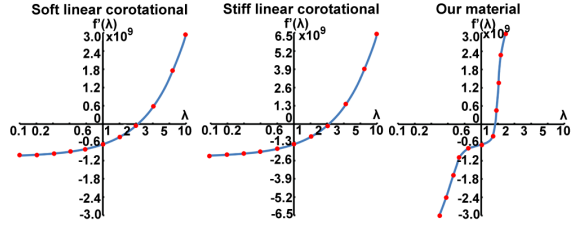


Figure 8: Material curves for the elephant example (Figure 2).

will be defined as m_1, m_2, m_3 . These axes need not be aligned with the world coordinates, can be chosen arbitrarily by the user and can vary from element to element if needed. Similar to the transversely isotropic materials presented in [Teran et al. 2003; Irving et al. 2004], we split the strain energy function Ψ into

$$\Psi = \Psi_{iso}(\lambda_1, \lambda_2, \lambda_3) + \Psi_{ortho}, \quad (18)$$

$$\Psi_{ortho} = w_1(\bar{\lambda}_1) + w_2(\bar{\lambda}_2) + w_3(\bar{\lambda}_3), \quad (19)$$

where Ψ_{iso} is isotropic strain energy (Equation 11), and $w_i(\bar{\lambda}_i)$ is the orthotropic energy term accounting for the stretch of the three orthotropic material axes, $\bar{\lambda}_i = \|Fm_i\|_2$. The first Piola stress tensor can be computed as in Equation 3 (here, $x \otimes y = xy^T$), where

$$\mathbf{P}(\hat{\mathbf{F}}) = \mathbf{P}_{iso}(\hat{\mathbf{F}}) + \sum_{i=1}^3 \hat{\mathbf{F}} \frac{w'_i(\bar{\lambda}_i)}{\bar{\lambda}_i} (\mathbf{V}^T m_i) \otimes (\mathbf{V}^T m_i). \quad (20)$$

The $\partial \mathbf{P}(\hat{\mathbf{F}}) / \partial \mathbf{F}$ can be further computed as

$$\begin{aligned} \frac{\partial \mathbf{P}(\hat{\mathbf{F}})}{\partial \mathbf{F}_{ij}} &= \frac{\partial \mathbf{P}_{iso}(\hat{\mathbf{F}})}{\partial \mathbf{F}_{ij}} + \sum_{i=1}^3 \left(\frac{\partial \hat{\mathbf{F}}}{\partial \mathbf{F}_{ij}} \frac{w'_i(\bar{\lambda}_i)}{\bar{\lambda}_i} (\mathbf{V}^T m_i) \otimes (\mathbf{V}^T m_i) + \right. \\ &\quad \left. + \hat{\mathbf{F}} \frac{w''_i(\bar{\lambda}_i) \bar{\lambda}_i - w'_i(\bar{\lambda}_i)}{\bar{\lambda}_i^2} \frac{\partial \bar{\lambda}_i}{\partial \mathbf{F}_{ij}} (\mathbf{V}^T m_i) \otimes (\mathbf{V}^T m_i) + \right. \\ &\quad \left. + \hat{\mathbf{F}} \frac{w'_i(\bar{\lambda}_i)}{\bar{\lambda}_i} \left(\left(\frac{\partial \mathbf{V}^T}{\partial \mathbf{F}_{ij}} m_i \right) \otimes (\mathbf{V}^T m_i) + (\mathbf{V}^T m_i) \otimes \left(\frac{\partial \mathbf{V}^T}{\partial \mathbf{F}_{ij}} m_i \right) \right) \right), \quad (21) \end{aligned}$$

$$\frac{\partial \bar{\lambda}_i}{\partial \mathbf{F}_{ij}} = \frac{1}{2\bar{\lambda}_i} m_i^T \frac{\partial \mathbf{F}^T \mathbf{F}}{\partial \mathbf{F}_{ij}} m_i, \quad \frac{\partial \mathbf{F}^T \mathbf{F}}{\partial \mathbf{F}_{ij}} = \mathbf{F}^{i,j} + (\mathbf{F}^{i,j})^T, \quad (22)$$

where $\partial \hat{\mathbf{F}} / \partial \mathbf{F}_{ij}, \partial \mathbf{V}^T / \partial \mathbf{F}_{ij}$ are as in Equations 7 and 9, and $\mathbf{F}^{i,j}$ is a matrix with all the elements 0, except the i -th row equals the j -th row of \mathbf{F} . The user selects the material directions m_j and edits the scalar derivative 1D functions w'_j that correspond to the material behavior along the material directions m_j , for $j = 1, 2, 3$. An increasing orthotropic material curve w'_j will make the material direction j stiffer, while a decreasing curve w'_j results in a softer material. We enforce positiveness of the energy function Ψ by constraining the modulation w'_j to remain smaller than the isotropic base. The transversely isotropic and isotropic materials are special cases where two and three of the w'_j curves are zero, respectively.

5 Results

In the elephant example (Figure 2), we create an isotropic nonlinear material for a jumping elephant (20,505 tets, 6,788 vertices, 7.0 fps, Intel Xeon 2x8 cores 2.9 GHz CPU, 32GB RAM). The feet, head and upper back follow a Maya rigged animation (using constraints), whereas the rest (trunk, ears, belly, tail) are simulated using a tetrahedral mesh. Within each of these four regions, we use a homogeneous material that follows the same material curve but is scaled so that the trunk is stiffer and the belly softer than the ears

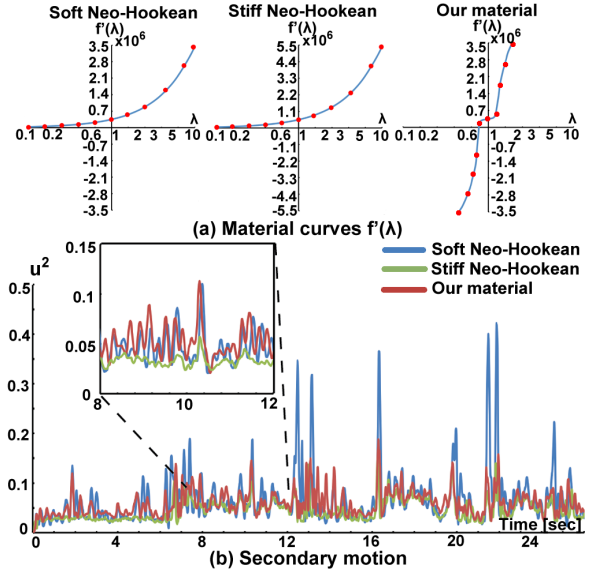


Figure 9: Material curves and secondary motion for the dancing wrestler example (Figure 1): (a) The designed material curve $f'(\lambda)$ is modeled based on the Neo-Hookean material. The designed material matches the soft Neo-Hookean material in small deformation region. (b) Magnitude of secondary motion across the frames. During the gentle motion, the soft Neo-Hookean material (blue) and our designed material (red) produce larger deformations and vibrations than the stiff Neo-Hookean material (green). For impulsive motions, the soft Neo-Hookean produces large spikes (visually severe deformations) while the designed material and the stiff Neo-Hookean can keep the deformation reasonable.

and tail. We first attempted to obtain reasonable results using the standard linear corotational material, by tuning its Young's modulus. However, the tuned parameter will affect the strain-stress relationship for the entire range of strains. If we set Young's modulus high, the motion is good during strong ground impacts, but is too stiff (nearly rigid) during the gentle phases of motion (gentle locomotion or ballistic motion). Conversely, if we decrease the Young's modulus, we then have the opposite situation where the dynamics are rich during the gentle phase, but are grossly enlarged during the impulsive phase. In our material, obtained by modeling the f' curve using splines (Figure 8), the f' curve is adjusted so that the elephant soft tissue exhibits good motion both under small deformations and large deformations. In the small deformation regime ($0.75 \leq \lambda \leq 1.3$), we set the f' curve to the same as in the linear corotational material, whereas for $\lambda \geq 1.3$ and $\lambda \leq 0.75$, we place the spline control points so as to increase the slope of the f' curve.

An alternative approach to achieving such an effect would be to segment the motion, then keyframe the stiffness of the material over time. However, this first requires segmenting the motion, which can be tedious. Further, the process of tuning Young's modulus over time can be tedious, and it only works for one motion. In our method, once the f' curve is set, the material can be applied to any other motion of that character, or other characters. Even more importantly, changing Young's modulus over time makes the system non-conservative; it is akin to adding a muscle to the object. This easily leads to visual artifacts since the dynamics are no longer conservative, as demonstrated in Figure 10. Another disadvantage of the keyframing method is that adjusting Young's modulus at a certain frame affects both compression and tension simultaneously. If the motion is good in compression while suboptimal in tension (or vice versa), it is not possible to fix it by adjusting Young's modulus.

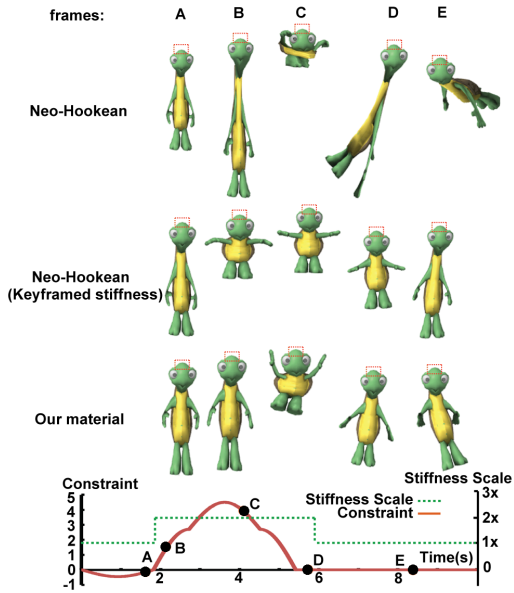


Figure 10: Keyframing stiffness over time does not work: The top of the turtle is constrained, undergoing gentle and rapid up-down motion, with gravity enabled (fourth row). Soft Neo-Hookean material produces severe deformations (first row). In the second row, we tried to avoid large deformation by keyframing stiffness. During the large deformation stage, stiffness is increased by $2\times$, so that the maximum stretched length matches that of our material. However, the dynamics are visually illogical. From A to B (stiffness increased), since the internal force jumps to a higher value, the turtle quickly compresses (muscle contraction). At C, the high stiffness destroys the damping and dynamics by making it behave rigidly. From D to E (stiffness restored), with damping, the turtle is stretched under gravity even longer at E than at D (muscle release). Our material, in turn, can produce quality motion (third row).

In the dancing wrestler example (7,767 tets, 2,717 vertices, 14.5 fps), we demonstrate these challenges further (Figure 1), as in this case, it is very difficult to even segment the motion. Under the Neo-Hookean material, it is impossible to have quality soft-tissue motion for all phases of motion, whereas our f' curve provides good dynamics both under gentle motion (walking and low jumps) and after abrupt events (jumping high, rapidly leaning forward). Figure 9 (b) demonstrates the temporal distribution of the deformations across the entire simulation by giving the 2-norm of deformation vectors.

Our third example is a soft solid sphere (10,611 tets, 2,340 vertices, 4.0 fps) whose top part is keyframed in an up-down motion (Figure 11). In this example, we demonstrate an intuitive relationship between the f' curve and the corresponding visual effects. Our design begins with the Neo-Hookean material (default material) and we only edit the f' curve. In the first curve, the tension region ($\lambda \geq 1$) is kept the same as the default material whereas in the compression region ($\lambda < 1$), our curve decreases much faster than the default curve, causing the material to resist compression. Visually, this manifests by the sphere being less flattened and the rim (the most compressed part) being thicker than under the default material. Note that volume preservation is enabled in both simulations, using h from Equation 16. Under large tensions, both materials are deformed to about equal length, consistent with the curves being equal in the tension region. The second designed material is the opposite to the first one: it keeps the compression curve same as in the default material, but stiffens under tension. Consequently, we observe that with this material, the sphere compresses (flattens) in the same way as the default material, but deforms less under stretching.

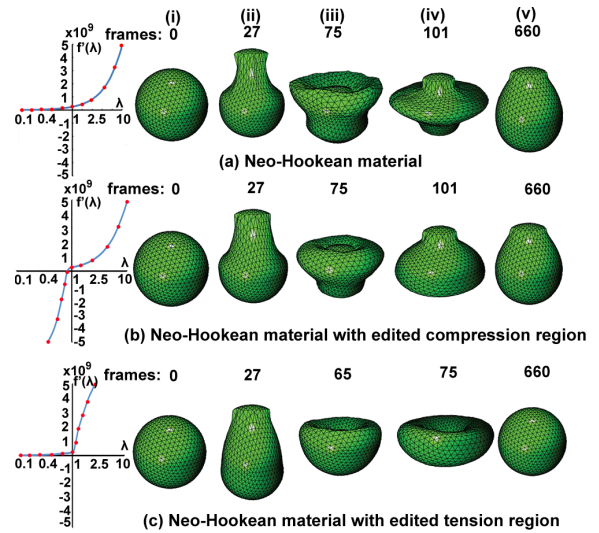


Figure 11: Dynamics of a solid sphere under varying materials. Materials (a) and (b) are the same under tension but (b) stiffens under compression. Materials (a) and (c) are the same under compression but (c) stiffens under tension. The top section of the sphere is constrained to undergo a scripted up-down motion. In column (ii), the material is stretching due to the upward motion of the constraints, and the tension-soft materials (a) and (b) produce a “neck”, unlike the tension-stiffer material (c). In column (iii), the simulation is in a compression stage, where we can see (a) and (c) producing a thinner rim than (b). This is because (b) is hard under compression, preventing excessive compression and resulting in a smoother shape. Column (iv) gives the most flattened shape in the compression stage. Material (b) is much less flattened while (a) and (c) are almost completely flattened in some regions. Material (c) compresses less than (a) (but more than (b)) because of the coupling between tension and compression. Column (iv) shows the equilibrium shape under gravity. Materials (a) and (b) produce similar deformations whereas (c) is stiffer and deforms less.

However, note that due to volume preservation, when the material stretches in a direction, it will compress in other directions. This effect introduces some weak coupling between compression and tension (columns (ii), (iii) and (iv) of Figure 11). Such visual effects are not practical with standard global materials, since both compression and tension regions are affected simultaneously.

Our spline tool can also design various materials exhibiting interesting dynamics. In Figure 12, we demonstrate a local interactive edit to f' to make the material stiffer under small deformations. Although such a material may not be practical in the real world, it can still be useful for animations to create interesting dynamics. This example demonstrates the local control property of our material editing tool. We can arbitrarily adjust the material in different strain regions to accommodate a specific dynamic purpose.

In our last example (Figure 14), we edit both the isotropic and orthotropic nonlinear material curves (armadillo model, 2,613 tets, 999 vertices, 24 fps). The three material axes are aligned with the world coordinates. We performed a comparison between the isotropic nonlinear, orthotropic nonlinear and linear corotational orthotropic materials [Li and Barbič 2014]. The isotropic part of the orthotropic nonlinear material is the same as in the isotropic nonlinear model. Compared to the linear model, the nonlinear materials stiffen quickly under large deformation. We designed the orthotropic material curves so that the m_1 direction is unmodified, but becomes softer and stiffer in the m_2 and m_3 directions, respectively.

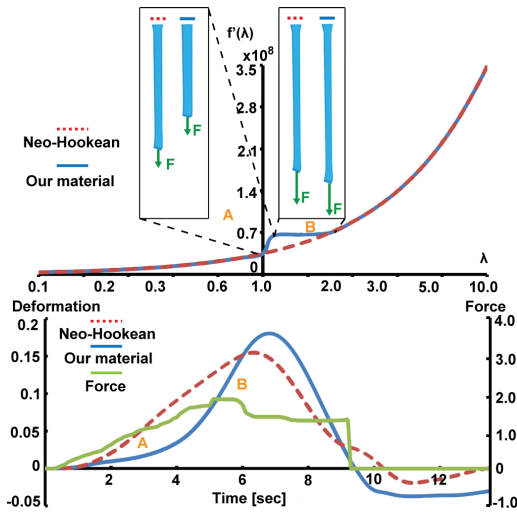


Figure 12: Local control of materials: Top: red dotted line is the f' curve for the Neo-Hookean material. Blue line is our edited material. In region A, we increased the slope of f' , followed by a plateau in region B. The two materials are equal everywhere else. Bottom: beam deformation under an interactive mouse force. Initially, our material is more difficult to stretch (region A), but after the deformation reaches region B, it deforms more easily. This happens because in region B, our material produces a smaller tangent stiffness matrix and therefore lower Rayleigh damping. This causes a higher velocity in region B for our material, making it stretch even longer than the Neo-Hookean material.

The Young’s moduli along the three material directions for linear corotational orthotropic material are chosen so that it approximately matches the orthotropic nonlinear material under small deformations. Due to linearity, the linear corotational orthotropic material produces severe deformations when pulled in the m_2 direction.

Spline locality enables materials that are less sensitive (more forgiving) to user interaction than global materials (see Figure 7). It is not necessary to precisely place the spline control points to get good results. Starting from the default material curve, the number of design iterations for all our isotropic examples was 3 or less. For complex models and motions, each material tuning iteration can be expensive. However, we can accommodate them by designing the material interactively on a coarse mesh and then applying it to the fine mesh, or any other mesh. We observed that when transferring the material to a fine mesh, only a small global rescale of the material curve is typically required (to accommodate the somewhat higher compliance of the fine mesh as it has more DOFs). There is no need to re-tune the entire curve. To accelerate the design process, one can use static solves before simulating dynamics. A set of characteristic static loads provides visual feedback on the material nonlinearity and can guide the user to adjust the curve accordingly (Figure 13).

We compared our SVD gradient simulation method to [Gao et al. 2009], which also defines and simulates the materials in the stretch-based space. Gao et al. [2009] computes the first Piola-Kirchhoff stress and stiffness matrix via symbolic differentiation as

$$P = \frac{\partial W}{\partial F} = \frac{\partial W}{\partial \lambda} \left(\frac{\partial \lambda}{\partial I_C} \frac{\partial I_C}{\partial F} + \frac{\partial \lambda}{\partial II_C} \frac{\partial II_C}{\partial F} + \frac{\partial \lambda}{\partial III_C} \frac{\partial III_C}{\partial F} \right). \quad (23)$$

However, $\frac{\partial W}{\partial F}$ and $\frac{\partial^2 W}{\partial F^2}$ are very complex expressions, and are infeasible to derive and implement manually. Instead, as in [Gao et al. 2009], we implemented these two functions in Mathematica and exported the results to C code. For the Ogden material, the resulting

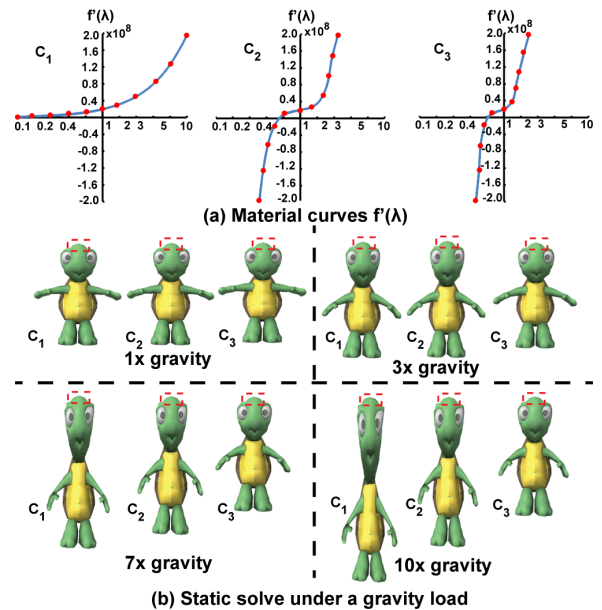


Figure 13: “Preview” of spline materials using static solves. We can solve for the static equilibrium shape under characteristic force loads (we use gravity). The user can either vary the force load under a fixed material, or edit the spline under a fixed static force load, to get a sense of the material nonlinearity.

C file was 22 Mb, and the C compiler took three hours to compile it. At runtime, we measured our method to be at least $35\times$ faster than [Gao et al. 2009]. Note that unlike in our method, the internal force computation in [Gao et al. 2009] is not continuous in the vicinity of multiple eigenvalues of F . We compared the stability of both methods. In addition to being $35\times$ faster, our method is also more stable by allowing at least $5\times$ larger timestep (Figure 4 (d)).

We also compared our SVD gradient simulator to the simulators of Teran et al. [Teran et al. 2005] and Stomakhin et al. [Stomakhin et al. 2012]. Neither of the methods showed any stability issues. We measured the timings to compute the internal forces and stiffness matrices, on the beam example, using a single thread for all methods. When comparing to [Teran et al. 2005] on a StVK material expressed using the invariants I_C, II_C, III_C , our method was approximately 25% faster. When comparing to [Stomakhin et al. 2012] on a corotational material expressed using $\lambda_1, \lambda_2, \lambda_3$ (Figure 4, (b)), our method was approximately 33% faster overall. The computation of dP/dF , which is the key difference between the two methods, was $2.2\times$ faster in our method.

6 Conclusion

We presented a method to simulate nonlinear materials using the principal stretches of the material. Design of materials in the space of principal stretches is intuitive and we show how to apply it to isotropic and anisotropic material design for soft-body simulation in computer animation. Our design method uses a simplified family of energies. Although this hypothesis is frequently used in engineering and in practice produces both useful materials and design freedom, there are materials that we cannot model. Our method accelerates state-of-the-art principal stretch simulators. A numerical threshold is required for the singular value decomposition. Although we demonstrated that the effect of this parameter is negligible, it would be interesting to design a method that completely avoids such thresholds. In our orthotropic model, we model shear as isotropic; **we do not include orthotropic shear terms**. The three

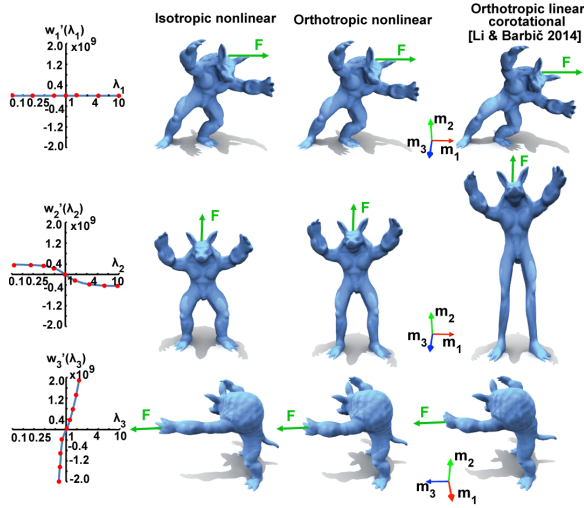


Figure 14: Orthotropic material design. The material directions m_1, m_2, m_3 are equal (top row), softer (middle row) and stiffer (bottom row) than the isotropic material. The nonlinear material stiffens under large deformations, whereas the linear material does not.

orthotropic “fibre-stretch” curves w_i can in practice model visually good orthotropic properties. **In order to simulate more accurate mechanical models, however, one could add three nonlinear shear material curves to Ψ_{ortho} .** Our method does not explicitly provide high-level assistance to the user, such as inferring materials from user-specified vertex constraints. In the future, we would like to explore such direct animation control. **It would be interesting to subject our spline control points to an optimization process, for example, to design materials that match some real-world experiments.** It would also be useful to extend our model to general anisotropic material and plastic deformations.

Acknowledgements: This research was sponsored in part by the National Science Foundation (CAREER-1055035, IIS-1422869), the Sloan Foundation, USC Annenberg Graduate Fellowship to Hongyi Xu, the James H. Zumberge Research and Innovation Fund at the University of Southern California, and a donation of two workstations by the Intel Corporation.

A Separable Material Energy Examples

Many standard global material models are expressible in the form of Assumption 11. The St.Venant-Kirchhoff material is

$$f(x) = \frac{1}{8}\lambda_{Lamé}(x^4 - 6x^2 + 5) + \frac{1}{4}\mu_{Lamé}(x^2 - 1)^2,$$

$$g(x) = \frac{1}{4}\lambda_{Lamé}(x^2 - 1), \quad h(x) = 0. \quad (24)$$

The Neo-Hookean material can be expressed as

$$f(x) = \frac{\mu_{Lamé}}{2}(x^2 - 1),$$

$$g(x) = 0, \quad h(x) = -\mu_{Lamé} \log x + \frac{\lambda_{Lamé}}{2}(\log x)^2. \quad (25)$$

The linear corotational material [Müller and Gross 2004] is

$$f(x) = \frac{1}{2}\lambda_{Lamé}(x^2 - 6x + 5) + \mu_{Lamé}(2 - 2x),$$

$$g(x) = \lambda_{Lamé}(x - 1) + \mu_{Lamé}(x - 1), \quad h(x) = 0. \quad (26)$$

B Bézier Spline Evaluation

We construct the global function f' using piecewise Bézier spline interpolation and extrapolation. For each segment k of the Bézier spline, four control points $x_k, a_k, b_{k+1}, x_{k+1}$ are required [Shoemake 1985], where

$$a_k = \begin{cases} x_k - \frac{1}{6}x_{k-1} + \frac{1}{6}x_{k+1} & \text{if } 1 < k \leq m \\ \frac{2}{3}x_1 + \frac{2}{3}x_2 - \frac{1}{3}x_3 & \text{if } k = 1 \end{cases} \quad (27)$$

$$b_k = \begin{cases} x_k + \frac{1}{6}x_{k-1} - \frac{1}{6}x_{k+1} & \text{if } 1 < k < m \\ \frac{2}{3}x_m + \frac{2}{3}x_{m-1} - \frac{1}{3}x_{m-2} & \text{if } k = m + 1, \end{cases} \quad (28)$$

are automatically constructed. During the simulation, given a current principal stretch $\lambda \in \mathbb{R}$, we find the spline segment containing λ using a linear search, $x_k \leq \lambda \leq x_{k+1}$, and compute the scalar spline parameter $\zeta = (\lambda - x_k)/(x_{k+1} - x_k) \in \mathbb{R}$. Because there are typically only a few segments (less than 10 in our examples), a linear search is sufficient, but could be replaced for a binary search tree for more complex curves. We then evaluate

$$f' = [\zeta^3 \quad \zeta^2 \quad \zeta \quad 1] \begin{bmatrix} -1 & 3 & -3 & 1 \\ 3 & -6 & 3 & 0 \\ -3 & 3 & 0 & 0 \\ 1 & 0 & 0 & 0 \end{bmatrix} \begin{bmatrix} x_k \\ a_k \\ b_{k+1} \\ x_{k+1} \end{bmatrix}, \quad (29)$$

$$f'' = \frac{df'}{du} \frac{du}{d\lambda} = \frac{df'}{du} / \frac{d\lambda}{du}, \quad (30)$$

where df'/du is evaluated by differentiating Equation 29 with respect to u . When the principal stretch is outside of $[\lambda_{\min}, \lambda_{\max}]$, we extrapolate the spline with a quadratic curve with C_1 continuity. The quadratic coefficient for extrapolation to $\lambda > \lambda_{\max}$ is kept positive ($\lim_{x \rightarrow \infty} f'(x) = \infty$), whereas for $\lambda < \lambda_{\min}$, we use a negative quadratic coefficient to resist compression. The time to evaluate the splines is negligible compared to the rest of the simulation.

References

- ALLARD, J., MARCHAL, M., COTIN, S., ET AL. 2009. Fiber-based fracture model for simulating soft tissue tearing. *Studies in health technology and informatics* 142, 13–18.
- BALL, J. 1976. Convexity conditions and existence theorems in nonlinear elasticity. *Archive for Rational Mechanics and Analysis* 63, 4, 337–403.
- BECKER, M., AND TESCHNER, M. 2007. Robust and efficient estimation of elasticity parameters using the linear finite element method. In *Simulation und Visualisierung Conf. (SimVis)*, 15–28.
- BICKEL, B., BAECHER, M., OTADUY, M., MATUSIK, W., PFISTER, H., AND GROSS, M. 2009. Capture and modeling of non-linear heterogeneous soft tissue. *ACM Trans. on Graphics (SIGGRAPH 2009)* 28, 3, 89:1–89:9.
- BONET, J., AND BURTON, A. 1998. A simple orthotropic, transversely isotropic hyperelastic constitutive equation for large strain computations. *Computer Methods in Applied Mechanics and Engineering* 162, 151–164.
- BONET, J., AND WOOD, R. D. 1997. *Nonlinear Continuum Mechanics for Finite Element Analysis*. Cambridge Univ. Press.
- BOWER, A. 2011. *Applied Mechanics of Solids*. Taylor & Francis.
- CAPELL, S., GREEN, S., CURLESS, B., DUCHAMP, T., AND POPOVIĆ, Z. 2002. Interactive skeleton-driven dynamic deformations. *ACM Trans. on Graphics (SIGGRAPH 2002)* 21, 3, 586–593.

- CARMICHAEL, A., AND HOLDAWAY, H. 1961. Phenomenological elastomechanical behavior of rubbers over wide ranges of strain. *Journal of Applied Physics* 32, 2, 159–166.
- CHAO, I., PINKALL, U., SANAN, P., AND SCHRÖDER, P. 2010. A Simple Geometric Model for Elastic Deformations. *ACM Trans. on Graphics (SIGGRAPH 2010)* 29, 3, 38:1–38:6.
- CIVIT-FLORES, O., AND SUSÍN, A. 2014. Robust Treatment of Degenerate Elements in Interactive Corotational FEM Simulations. *Computer Graphics Forum* 33, 6, 298–309.
- DRUCKER, D. C. 1957. A definition of stable inelastic material. Tech. rep., DTIC Document.
- GAO, Z., KIM, T., JAMES, D. L., AND DESAI, J. P. 2009. Semi-automated soft-tissue acquisition and modeling for surgical simulation. In *Proc. of the 5th IEEE Int. Conf. on Automation Science and Engineering*, 268–273.
- HAHN, F., THOMASZEWSKI, B., COROS, S., SUMNER, R., AND GROSS, M. 2013. Efficient simulation of secondary motion in rig-space. In *Symp. on Computer Animation (SCA)*, 165–171.
- HERNANDEZ, F., CIRIO, G., PEREZ, A., AND OTADUY, M. 2013. Anisotropic strain limiting. In *Proc. of Congreso Español de Informática Gráfica*, vol. 2.
- IRVING, G., TERAN, J., AND FEDKIW, R. 2004. Invertible Finite Elements for Robust Simulation of Large Deformation. In *Symp. on Computer Animation (SCA)*, 131–140.
- KIKUUE, R., TABUCHI, H., AND YAMAMOTO, M. 2009. An edge-based computationally efficient formulation of saint venant-kirchhoff tetrahedral finite elements. *ACM Trans. on Graphics* 28, 1, 1–13.
- LEE, H.-P., AND LIN, M. 2012. Fast optimization-based elasticity parameter estimation using reduced models. *The Visual Computer* 28, 6-8, 553–562.
- LI, Y., AND BARBIČ, J. 2014. Stable orthotropic materials. In *Symp. on Computer Animation (SCA)*, 41–46.
- LI, S., HUANG, J., DE GOES, F., JIN, X., BAO, H., AND DESBRUN, M. 2014. Space-time editing of elastic motion through material optimization and reduction. *ACM Trans. on Graphics (SIGGRAPH 2014)* 33, 4, 108:1–108:10.
- MCADAMS, A., ZHU, Y., SELLE, A., EMPEY, M., TAMSTORF, R., TERAN, J., AND SIFAKIS, E. 2011. Efficient elasticity for character skinning with contact and collisions. *ACM Trans. on Graphics (SIGGRAPH 2011)* 30, 4, 37:1–37:11.
- MOONEY, M. 1940. A theory of large elastic deformation. *Journal of applied physics* 11, 9, 582–592.
- MÜLLER, M., AND GROSS, M. 2004. Interactive Virtual Materials. In *Proc. of Graphics Interface 2004*, 239–246.
- O'BRIEN, J., AND HODGINS, J. 1999. Graphical Modeling and Animation of Brittle Fracture. In *Proc. of ACM SIGGRAPH 1999*, 111–120.
- OGDEN, R. W. 1997. *Non-linear elastic deformations*. Courier Dover Publications.
- PAPADOPOULOU, T., AND LOURAKIS, M. I. 2000. Estimating the Jacobian of the singular value decomposition: Theory and application. In *European Conf. on Computer Vision*, 554–570.
- PARKER, E. G., AND O'BRIEN, J. F. 2009. Real-time deformation and fracture in a game environment. In *Symp. on Computer Animation (SCA)*, 156–166.
- PEREZ, A., CIRIO, G., HERNANDEZ, F., GARRE, C., AND OTADUY, M. 2013. Strain limiting for soft finger contact simulation. In *World Haptics Conference (WHC)*, 2013, 79–84.
- PICINBONO, G., DELINGETTE, H., AND AYACHE, N. 2001. Non-linear and anisotropic elastic soft tissue models for medical simulation. In *IEEE Int. Conf. on Robotics and Automation 2001*.
- SHOEMAKE, K. 1985. Animating rotation with quaternion curves. In *Proc. of ACM SIGGRAPH 1985*, 245–254.
- SIFAKIS, E., AND BARBIČ, J. 2012. FEM simulation of 3D deformable solids: A practitioner's guide to theory, discretization and model reduction. In *SIGGRAPH 2012 Course Notes*.
- SIFAKIS, E., NEVEROV, I., AND FEDKIW, R. 2005. Automatic determination of facial muscle activations from sparse motion capture marker data. *ACM Trans. on Graphics (SIGGRAPH 2005)* 24, 3, 417–425.
- STOMAKHIN, A., HOWES, R., SCHROEDER, C., AND TERAN, J. M. 2012. Energetically consistent invertible elasticity. In *Symp. on Computer Animation (SCA)*, 25–32.
- SUSSMAN, T., AND BATHE, K.-J. 2009. A model of incompressible isotropic hyperelastic material behavior using spline interpolations of tension-compression test data. *Communications in Numerical Methods in Engineering* 25, 1, 53–63.
- TALBOT, H., MARCHESSEAU, S., DURIEZ, C., SERMESANT, M., COTIN, S., AND DELINGETTE, H. 2013. Towards an interactive electromechanical model of the heart. *Interface focus* 3, 2, 20120091.
- TEN THIJE, R., AKKERMAN, R., AND HUÉTINK, J. 2007. Large deformation simulation of anisotropic material using an updated lagrangian finite element method. *Computer methods in applied mechanics and engineering* 196, 33, 3141–3150.
- TERAN, J., BLEMKER, S., HING, V. N. T., AND FEDKIW, R. 2003. Finite volume methods for the simulation of skeletal muscle. In *Symp. on Computer Animation (SCA)*, 68–74.
- TERAN, J., SIFAKIS, E., IRVING, G., AND FEDKIW, R. 2005. Robust Quasistatic Finite Elements and Flesh Simulation. In *Symp. on Computer Animation (SCA)*, 181–190.
- TWIGG, C., AND KAČIĆ-ALESIĆ, Z. 2010. Point cloud glue: constraining simulations using the procrustes transform. In *Symp. on Computer Animation (SCA)*, 45–54.
- VALANIS, K., AND LANDEL, R. 1967. The strain-energy function of a hyperelastic material in terms of the extension ratios. *Journal of Applied Physics* 38, 7, 2997–3002.
- WANG, H., O'BRIEN, J. F., AND RAMAMOORTHY, R. 2011. Data-driven elastic models for cloth: modeling and measurement. *ACM Trans. on Graphics (SIGGRAPH 2011)* 30, 4, 71:1–71:11.